Published in final edited form as:
J Am Chem Soc. 2006 May 24; 128(20): 6657–6668. doi:10.1021/ja0584626.

^{1}H NMR study of the magnetic properties and electronic structure of the hydroxide complex of substrate-bound heme oxygenase from *Neisseria meningitidis*; Influence of the axial water deprotonation on the distal H-bond network

Li-Hua Ma†, **Yangzhong Liu**†, **Xuhang Zhang**‡, **Tadashi Yoshida**‡, and **Gerd N. La Mar**†,*

†*Department of Chemistry, University of California, Davis, CA 95616*

‡*Department of Biochemistry, Yamagata University School of Medicine, Yamagata 990-9585, Japan*

Abstract

The substrate and active site residues of the low-spin hydroxide complex of the protohemin complex *Neisseria meningitidis* heme oxygenase, HO, *Nm*HO, have been assigned by saturation transfer between the hydroxide and previously characterized aquo complex. The available dipolar shifts allowed the quantitation of both the orientation and anisotropy of the paramagnetic susceptibility tensor. The resulting positive sign, and reduced magnitude of the axial anisotropy relative to the cyanide complex, dictate that the orbital ground state is the conventional 'd_π' (d_{xy} ^{2}(d_{xz}, d_{yz})^3); and not the unusual 'd_{xy}' (d_{xz} $^2d_{yz}$ $^2d_{xy}$) orbital ground state reported for the hydroxide complex of the homologous heme oxygenase from *Pseudomonas aeruginosa*, (Caignan, G., Deshmukh, R., Zeng, Y., Wilks, A., Bunce, R.A., Rivera, M.; J. Am. Chem. Soc. 125, 11842-11852) and proposed as a signature of the HO distal cavity. The conservation of slow labile proton exchange with solvent from pH 7.0 to 10.8 confirms the extraordinary dynamic stability of *Nm*HO complexes. Comparison of the diamagnetic contribution to the labile proton chemical shifts in the aquo and hydroxide complexes reveals strongly conserved bond strengths in the distal H-bond network, with the exception of the distal His53 $N_{\varepsilon 1}H$. The iron-ligated water is linked to His53 primarily by a pair of non-ligated, ordered water molecules which transmit the conversion of the ligated H-bond donor (H_2O) to a H-bond acceptor (OH^-), thereby increasing the H-bond donor strength of the His53 side chain.

Keywords

N. meningitidis heme oxygenase; magnetic anisotropy; heme electronic ground state; H-bonding

INTRODUCTION

Heme oxygenase, HO[1], is a non-metal enzyme that uses protohemin, PH, as both cofactor and substrate to generate biliverdin, iron and CO.[1-6] HOs are widely distributed. In mammals they maintain iron homeostasis,[7] produce the precursor to the powerful antioxidant,[4, 8] biliverdin, and generate CO as a potential neural messenger.[8, 9] In plants and cyanobacteria, HOs generate the linear tetrapyrroles as precursors to light-harvesting pigments. [10] The HOs identified for

AUTHOR EMAIL ADDRESS lamar@chem.ucdavis.edu.

[1]ABBREVIATIONS: HO, heme oxygenase; *Nm*HO, *Neisseria meningitidis* heme oxygenase; NOESY, two-dimensional nuclear Overhauser spectroscopy; TOCSY, two-dimensional total correlation spectroscopy; Dss, 2,2-dimethyl-2-silapentane-5-sulfonate; PH, protohemin;

a number of pathogeneic bacteria[11-13] appear to have as their major role the "mining" of iron to infect a host. [3, 5] Two such HOs of interest here are *Neisseria meningitidis*, *Nm*HO (also called HemO [12, 14, 15]) and *Pseudomonas aeruginosa*, *Pa*HO [13, 16, 17]. A common mechanism, worked out on the mammalian HOs, appears operative in the various HOs.[2-4, 18] The resting-state substrate complex, HO-PH-H_2O, is first reduced, after which O_2 is ligated.[19] Upon adding another electron and a proton, the ferric hydroperoxy species (Figure 1A) is formed [20-22] which attacks one of the meso-carbons to yield the initial meso-hydroxy-PH intermediate. The hydroperoxy species as the hydroxylation agent in HO is in contrast to the active ferryl species in cytochromes P450 and peroxidases.[4, 20] The structural basis for stabilizing the hydroperoxy species and destabilizing O-O bond cleavage is of considerable current interest.[22-24] While mechanistic studies are consistent with electrophilic rather than nucleophilic attack on the meso carbon, [20] a free radical contribution has not been ruled out.[6, 25]

Due to the instability of the oxy and hydroperoxy species at ambient temperatures,[22-24, 26] structural characterization by crystallography or ^{1}H NMR, with one exception, [26] has had to resort to model complexes, ferrous HO-PH-NO[15, 27] and HO-PH-CO[28] and ferric HO-PH-N_3 and HO-PH-CN[28] for X-ray crystallography and the ferric HO-PH-CN[16, 29-34] (or HO-PH-N_3) complexes for NMR as models for ferrous HO-PH-O_2 complex. The diverse crystal structures of mammalian[27, 28, 35, 36] and bacterial[14, 15, 17, 26, 37] HOs reveal a common fold where the placement of the distal helix close to the heme plane blocks three of the four meso-positions from attack by Fe^{+3}-OOH, and steric interaction of the ligand directly with the distal helix backbone "orients/tilts" the axial ligand towards the fourth, unblocked meso-position. The crystal structures, moreover, locate a set of three conserved, non-ligated, ordered water molecules in the distal pocket that are implicated in stabilizing the Fe^{+3}-OOH species and likely serve as the proton conduit to the active site.[15, 26, 27, 36] Solution ^{1}H NMR studies have shown[31-34] that HOs possess an extended H-bond network in the distal pocket with some stronger than usual H-bonds which serve as a scaffold for not only the three "catalytically" implicated water, but also to numerous other ordered water molecules. Based on the sum rule for g values applied to the ENDOR-detected HO ferric hydroperoxy species [22] and comparison to structurally characterized model compounds, [38, 39] it has been proposed that, due to the unusual distal H-bonding interaction,[6] the low-spin HO-PH-OOH complex exists in a 'd_{xy}' ($d_{xz}{}^2 d_{yz}{}^2 d_{xy}$) rather than the more conventional 'd_π' ($d_{xy}{}^2 (d_{xz}, d_{yz})^3$) orbital ground state, with the PH exhibiting significant ruffling.[38-40] This "ruffling" in the 'd_{xy}' ground state could result in large unpaired spin density (observed by ^{13}C NMR) appearing at the meso-carbons. Such a 'd_{xy}' ground state has been viewed as a unique self-activating role of PH in HOs. [6, 40]

The reactive HO-PH-OOH species is sufficiently stable for spectroscopic study only at cryogenic temperatures.[22-24] However, solution ^{13}C NMR studies on *Pa*HO-PH-OH containing ^{13}C labeled PH revealed [40] large meso-carbon spin densities indicative [38, 39] of the d_{xy} orbital ground state, suggesting that the HO-PH-OH complex may serve as a valid model for the unusual distal H-bond interaction that stabilizes the 'd_{xy}' ground state in *Pa*HO-PH-OOH. Confirming the d_{xy} ground state by ^{13}C NMR, however, requires selective ^{13}C labeling that is readily achievable for PH,[40] but would require total synthesis for modified substrates whose altered basicity would modulate[41-44] the axial ligand H-bonding interaction between the distal water molecules and H-bonding network. The 'd_{xy}' ground state, however, possesses additional magnetic resonance signatures which have more general applicability to diverse HO complexes. Thus the 'd_π' and 'd_{xy}' orbital ground states differ characteristically [38, 39, 45, 46] in the *sign of their axial anisotropy*, $\Delta\chi_{ax}$. While low-spin iron(III) in either orbital state exhibits a rhombic χ tensor (or g tensor), the axial $\Delta\chi_{ax}$ is always much larger than $\Delta\chi_{rh}$ by factors ~3 and dominates the dipolar fold of the iron. The determination of the sign of the axial anisotropy could be most directly determined by EPR, but would require single

crystals that should allow detection at ambient temperatures. The former is difficult, the latter not possible because of the rapid electron spin relaxation at all but cryogenic temperatures. However, the sign (and magnitude) of anisotropy of χ can be directly determined by solution ^{1}H NMR using experimental dipolar shifts, δ_{dip}, induced in the protein matrix by the anisotropic χ tensor. This shift is given by: [47-49]

$$\delta_{dip}=(24\pi N_A)^{1}[\,2\Delta\chi_{ax}(3\cos^2\theta'1)R^3+3\Delta\chi_{rh}(\sin^2\theta'\cos2\Omega)R^3]\Gamma(\alpha,\beta,\gamma) \quad (1)$$

where x', y', z' (R, θ', Ω') are proton positions in an arbitrary, iron-centered coordinate system, $\Delta\chi_{ax}$ and $\Delta\chi_{rh}$ are the axial (χ_{zz}- 1/2(χ_{xx} + χ_{yy})) and rhombic anisotropies (χ_{xx}-χ_{yy}), and Γ(α, β, γ) is the Euler rotation that converts the reference coordinates, x', y', z', into the magnetic coordinate system, x, y, z, where χ is diagonal. The anisotropies and orientation of χ can be determined experimentally if sufficient experimental dipolar shifts can be assigned and valid crystal coordinates are available to generate x', y', z'. The anisotropy and orientation of numerous low-spin ferrihemoproteins in the conventional S = 1/2, d_π ground state have been determined and they have the common property[38, 49] of large positive $\Delta\chi_{ax} > 2 \times 10^{-8}$ m^3/mol, and much smaller rhombic anisotropies with $|\chi_{ax}/\Delta\chi_{rh}|$ ~3-4.

We have been engaged in a study of the functionally relevant molecular and electronic structural information-content of the NMR spectra for a range of paramagnetic substrate complexes of both mammalian [30-32] and bacterial [33, 34, 50] HOs. A particularly attractive candidate is the HO from the pathogeneic bacterium *Neisseriae meningitidis*, *Nm*HO, a ~210 residue enzyme.[3, 12] The distal ligand in *Nm*HO complex interacts with the distal water molecules[14, 15] that, in turn, interact with a series of amino acid residues, either as acceptor or donors. *Nm*HO has the desirable properties of populating essentially a single PH orientation about the α-,γ-meso axis, that is the same in both solution [6, 34, 50] and crystals [14, 15] and which displays superior resolution that has allowed ^{1}H NMR characterization of a significant fraction of the complex in both the low-spin[34], *Nm*HO-PH-CN, and the high-spin,[50] *Nm*HO-PH-H_2O, complexes. ^{1}H NMR spectra of only one hydroxide HO complex, *Pa*HO-PH-OH, have been reported[40] for which the heme signals were assigned by ^{13}C labeling. No information was provided on the protein matrix that could shed light on the sign or magnitude of the magnetic anisotropy.

We report here on the thermodynamics and dynamics of the *Nm*HO-PH-H_2O ⇔ *Nm*HO-PH-OH interconversion and provide the characterization of the electronic/magnetic properties of the latter complex. The results indicate that *Nm*HO-PH-OH possesses large positive axial anisotropy that dictates it exists in the 'd_π' ground state. In addition to characterizing the electronic/magnetic properties of the *Nm*HO-PH-OH complex, we investigate the manner in which the H-bond donor in the distal pocket responds to conversion of the axial H-bond donor, ligated water (water *a* in Figure 1B) to a non-ligated water *b*, to an axial H-bond acceptor OH^- that serves as a H-bond acceptor to water *b*.

EXPERIMENTAL

Sample preparation

The apo-*Nm*HO samples used in this study are the same as described in detail previously. [34] Stoichiometric amounts of protohemin, PH (Figure 2), dissolved in 0.1 M KOH in ^1H_2O were added to apo-*Nm*HO in phosphate buffered (50 mM, pH 7.0). The substrate complex was purified by column chromatography on Sephadex G25 and yielded samples ~3 mM in *Nm*HO-PH-H_2O at pH 7.0. Samples in ^1H_2O were converted to ^2H_2O by column chromatography. [51] Sample pH for reference spectra in range 7.0 to 10.8 was altered by adding incremental 0.1 M KO^2H in ^2H_2O solution to *Nm*HO-PH-^2H_2O in ^2H_2O, 50 mM phosphate at 25°C. For long-term (>~24 h) 2D NMR spectra, samples were buffered at the desired pH with phosphate (pH

7.0 to 8.7) or bicarbonate (pH 9.1 to 10.8). The pH values in ^2H_2O are uncorrected for isotope effects.

NMR spectroscopy

^1H NMR data were collected on a Bruker AVANCE 500 and 600 spectrometers operating at 500 and 600 MHz, respectively. Reference spectra were collected in ^2H_2O over the temperature range 15-35°C at both a repetition rate of 1 s^{-1} over 40 ppm spectral width and at 5 s^{-1} over a 200 ppm band width. Steady-state, magnetization-transfer (NOE or exchange) difference spectra were generated from spectra with on-resonance, and off-resonance saturation of the desired signals; to detect exchange with H_2O, selective 3:9:19 excitation was used.[52] Chemical shifts are referenced to 2,2-dimethyl-2-silapentane-5-sulfonate (DSS) through the water resonance calibrated at each temperature. Non-selective T_1s were determined by the standard inversion-recovery pulse sequence and estimated from the null point. 600 MHz NOESY [53] spectra (mixing time 40 ms; repetition rate 2 s^{-1}) and 500 MHz Clean-TOCSY (to suppress ROESY response [54]) spectra (25°, 35°C, spin lock 25 ms) using MLEV-17 [55] were recorded over a bandwidth of 25 KHz (NOESY) and 12 KHz (TOCSY) with recycle times of 500 ms and 1s, using 512 t1 blocks of 128 and 256 scans each consisting of 2048 t2 points. 2D data sets were processed using Bruker XWIN software on a Silicon Graphics Indigo workstation. The processing consisted of 30°- or 45°-sine-squared-bell-apodization in both dimensions, and zero-filling to 2048 × 2048 data points prior to Fourier transformation.

Magnetic axes determination

The location of the magnetic axes was determined by finding the Euler rotation angles, Γ (α,β,γ), that rotate the crystal-structure based, iron-centered reference coordinate system, x', y', z', into the magnetic coordinate system, x, y, z, where the paramagnetic susceptibility tensor, χ, is diagonal where α, β, γ are the three Euler angles. [34, 47-50] The angle β dictates the tilt of the major magnetic axis, z, from the heme normal z', α reflects the direction of this tilt, and is defined as the angle between the projection of the z axis on the heme plane and the x' axis (Figure 2), and κ ~ α+γ is the angle between the projection of the x, y axes onto the heme plane and locates the rhombic axes (Figure 2). In the present case, we consider the tensor to be axially symmetric, so that $\Delta\chi_{rh} = 0$, and γ becomes irrelevant. The magnetic axes were determined by a least-square search for the minimum in the error function, F/n: [34, 47-50]

$$F/n=\sum_{i=1}^{n}|\delta_{dip}(obs) - \delta_{dip}(calc)|^2, \quad (2)$$

with observed dipolar shift, $\delta_{dip}(obs)$ given by:

$$\delta_{dip}(obs)=\delta_{DSS}(obs)\,\delta_{DSS}(dia), \quad (3)$$

where $\delta_{DSS}(obs)$ and $\delta_{DSS}(dia)$ are the chemical shifts, in ppm, referenced to DSS, for the paramagnetic *Nm*HO-PH-OH complex and an isostructural diamagnetic complex, respectively. In the absence of an experimental $\delta_{DSS}(dia)$ for the latter, it may be reasonably estimated [56, 57] from the available molecular structure [14] and available computer programs, [56, 57] as described previously for *Nm*HO-PH-CN [34] and *Nm*HO-PH-H_2O. [50]

RESULTS

pH titration

The influence of solution pH on the resolved portions of the 500 MHz ^1H NMR spectra of *Nm*HO-PH-H_2O in ^2H_2O in the pH range 8.0-10.8 is illustrated in Figure 3. The loss of intensity

in Figure 3A-3E, without concomitant line-broadening, of the assigned [50] heme methyl peaks in the 60-80 ppm window for high-spin *Nm*HO-PH-H_2O, and the appearance of two resolved, apparent heme methyl peaks in the 18-20 ppm window typical for the expected low-spin *Nm*HO-PH-OH complex, [49] dictate that the deprotonation/protonation of the exogenous ligand is slow on the NMR time scale. [58] In concert with this observation, all signals, including ones for inconsequentially relaxed protons and with only 0.1 ppm shift difference in the two species, similarly exhibited slow exchange, indicating the exchange rate is $<10^3$ s^{-1}. The sum of the intensities of an assigned [50] low-field heme methyl peak of *Nm*HO-PH-H_2O and that of the proposed (see below) heme methyl peak of *Nm*HO-PH-OH in the pH titration in ^2H_2O remained constant relative to the intensity of the diamagnetic envelope, within the experimental uncertainty of ~15%. This dictates that only two species are detectably populated, and leads to the Henderson-Hasselbalch plot in Figure 4 (open circles). The data of the strongly alkaline pH are likely suspect due to generation of a detectable third species above pH 10.2. However, the integration of the spectra in Figure 4 in the pH range 9.1 to 10.5 allows the estimate of the pK as 9.8 in ^2H_2O. The single spectrum at pH 10.2 in ^1H_2O, results in the filled marker in Figure 4, and indicates that the pK in ^1H_2O is ~0.4 units lower on the pH scale, or pK(^1H_2O) ~9.4.

The dominant *Nm*HO-PH-OH complex at pH 10.5 and 10.8 exhibited T_1s ~8-9 ms for the two resolved low-field heme methyl peaks, and T_1s ~7-10 ms for the apparent composite peak centered near 15 ppm (data not shown), which is assumed to arise from α-protons from the propionates and vinyl groups. At these alkaline pH values, exchange-transfer contributes negligibly to the effective T_1s, dictating that they are the true T_1s in the hydroxide complex. The upfield shoulder of the *Nm*HO-PH-OH spectrum at pH 10.5 exhibits one rapidly relaxed single proton peak with T_1s ~12 ms (not shown, see Supporting Information) that has no detectable NOESY cross peak. The upfield resonance position and relaxation rate are consistent with expectations for a vinyl H_β.[49]

Heme methyl assignments for *Nm*HO-PH-OH

Saturation of the assigned low-field methyl peaks[50] for the high-spin *Nm*HO-PH-H_2O complex in ^2H_2O at pH 8.9 results in the saturation-transfer-difference[58] spectra illustrated in Figures 3F-3H. These lead to the unambiguous assignment of the resolved $8CH_3$ (Figure 3F) and $3CH_3$ (Figure 3G) signals of *Nm*HO-PH-OH, and locate the $5CH_3$ signal (Figure 3H) at the low-field edge of the aromatic envelope. Saturation of the $1CH_3$ peak in *Nm*HO-PH-H_2O failed to reveal any clear signal attributable to $1CH_3$ in *Nm*HO-PH-H_2O and it is likely under the weak off-resonance saturation of the diamagnetic envelope resulting from the strong saturation field necessary to saturate the high-spin complex peak. Hence we conclude $1CH_3$ is located within the 1-7 ppm window.

The effect of temperature (not shown, see Supporting Information) on the chemical shifts for the resolved *Nm*HO-PH-OH methyl peak reveals weak Curie behavior for $3CH_3$ peak (apparent intercept at $T^{-1} = 0$ of 19 ppm), and weak anti-Curie behavior for the $8CH_3$ peak (apparent intercept at $T^{-1} = 0$ of 30 ppm).

Residue assignment protocols

All 2D spectra (both NOESY and TOCSY) with more than ~10% *Nm*HO-PH-OH present (above pH ~8.5) exhibited cross peaks that were strongly dominated by chemical exchange between *Nm*HO-PH-H_2O and *Nm*HO-PH-OH. This strong dominance of exchange cross peaks is obvious for resolved resonances where such cross peaks are instantly recognizable, as illustrated for the low-field spectral window in Figure 5. Brackets above the reference trace over the 2D map in Figure 5 connect the two sets of resonances (relative intensities ~3:1) for *Nm*HO-PH-OH and *Nm*HO-PH-H_2O, where the resonances of the latter complex have been

assigned previously.[50] In Figure 5, as in the following Figures 6-8, direct exchange cross peaks are labeled by asterisks (*), with the *Nm*HO-PH-OH and *Nm*HO-PH-H_2O frequencies marked by solid and dashed lines, respectively. Peaks are labeled by residue number and position, except for peptide NHs, which are labeled solely by residue number. Exchange-transferred NOESY cross peaks (*i.e.*, an NOE to a *Nm*HO-PH-H_2O proton *i*, that it is transferred to the same proton, *i*, in the *Nm*HO-PH-OH complex), are labeled by the pound marker (#). The NOESY spectrum in Figure 5 is dominated not only by direct exchange cross peaks (marked *), but also by exchange-transferred NOESY cross peaks (marked #) in ^1H_2O solution. For example, the *Nm*HO-PH-OH His141 $N_\delta H$ signal at 13.35 ppm (solid lines in Figure 5A) exhibits a *direct exchange cross peak* not only to the $N_{\delta 1}H$ in the *Nm*HO-PH-OH complex at ~10.8 ppm, but also to the 141NH of *Nm*HO-PH-H_2O (marked by #) at 10.4 ppm.

Figures 6A-6C present the reference spectra and the pertinent portions of the NOESY spectra for the upfield resolved spectral window as a function of increasing pH. Even at pH 7.2 (~3% *Nm*HO-PH-OH), exchange cross peaks can be detected (Figure 6A'), while at pH 8.7 (~12% *Nm*HO-PH-OH) exchange cross peaks are as intense as any intramolecular NOESY cross peaks (Figure 6B'). At pH 10.2 (~75-80% *Nm*HO-PH-OH; see Figure 6C'), by far the strongest cross peaks still originate from exchange. Thus with significant population of both isomers, a typical 2D map was dominated by exchange cross peaks that strongly obscure intramolecular NOESY cross peaks. It was not possible to identify a set of conditions (pH, temperature, mixing time) which provided a map that is dominated by the desired intramolecular cross peaks for the *Nm*HO-PH-OH complex. However, the above results suggest an approach where we inspect 2D maps as a function of pH, in which the appearance of new cross peaks with increasing pH can be uniquely attributed to exchange peaks to the same proton in the *Nm*HO-PH-OH complex.

Low-field resolved resonances in the H-bond network

Since the *Nm*HO-PH-H_2O cross peaks have been uniquely assigned[50] in *Nm*HO-PH-H_2O at a sufficiently low pH that exchange cross peak intensity is negligible, the identical assignments are trivially achieved for *Nm*HO-PH-OH complex, as shown in Figure 5. It is noted that, while most backbone NHs exhibit small to modest chemical shift differences between the two complexes, those of several side chains, particularly the His53 $N_{\varepsilon 1}H$ and Trp153 $N_\varepsilon H$, exhibit substantial chemical shift differences. The chemical shifts for labile protons in *Nm*HO-PH-OH are listed in Table 1, where they can be compared to the previously reported [34] values for *Nm*HO-PH-H_2O.

High-field resolved hyperfine shifted residues

The upfield portion of the NOESY spectrum with increasing pH (Figure 6) clearly leads to the assignment in *Nm*HO-PH-OH of each of the resolved upfield signals that had been previously assigned [50] in *Nm*HO-PH-H_2O. It is noted that in some cases, the exchange peak (marked by *) partially overlaps an intramolecular NOESY cross peak for *Nm*HO-PH-H_2O (*i.e.*, Val22 γ2/β NOESY cross peak (Figure 6A') and Val22 γ2 exchange cross peaks to *Nm*HO-PH-OH (Figures 6B', 6C')). Moreover, the appearance of very weak cross peak at pH 7.2 (Figure 6A), which increase strongly at higher pH (Figures 6B', and 6C'), allows the connection between the two complexes of the two resolved methyls in the *Nm*HO-PH-OH complex (Leu15 $C_{\delta 2}H_3$ and M_X), with an unassigned methyl peak (designated M_x) at -0.22 ppm in *Nm*HO-PH-OH, but 0.37 ppm in *Nm*HO-PH-H_2O. Since M_X in *Nm*HO-PH-OH exhibits insignificant hyperfine shifts (negligible temperature dependence), its assignment was not pursued further. The chemical shifts for residues with significant dipolar shifts (>|0.25| ppm) in *Nm*HO-PH-OH are listed in Table 2, and the data for the remaining assigned residues are listed in Supporting Information.

Non-resolved hyperfine-shifted resonances

Increasing the pH toward the alkaline region in ^2H_2O results in the detection of new cross peaks (due to exchange), and intensity increases with pH, for three key, dipolar shifted, aromatic residues assigned[34] in *Nm*HO-PH-H_2O, as illustrated at pH 8.7 in Figure 7. Exchange cross peaks (marked *) from the well-resolved ring protons of Phe125 in *Nm*HO-PH-H_2O identify all of the protons in *Nm*HO-PH-OH. Similar cross peaks are also observed for the $C_\zeta H$ and $C_\varepsilon Hs$ of Phe52 (marked by *); the $C_\delta Hs$ peak was found[34] very broad in *Nm*HO-PH-H_2O, which accounts for its undetectability in Figure 7. Lastly, an exchange cross peak also identifies the Tyr112 $C_\delta H$ cross peak (marked by *). It is noteworthy that the various ring chemical shifts for each Phe52 and Phe125 in the *Nm*HO-PH-OH complex are sufficiently close to each other so as to preclude the resolution of the intra-ring NOESY cross peaks in the pure *Nm*HO-PH-OH complex. The chemical shift for residues in *Nm*HO-PH-OH with significant dipolar shifts (> |0.25| ppm) are listed in Table 2, and the data for the remaining assigned residues are listed in Supporting Information.

Tyr184 ring protons exhibited very broad signals whose NOESY cross peak was marginally detectable in the *Nm*HO-PH-H_2O complex. [50] Its exchange cross peaks to *Nm*HO-PH-OH are not detectable at pH 8.7, but at pH 10.5, where *Nm*HO-PH-OH with narrower lines, is the dominant species, the ring exchange peaks are readily detected (Figure 8A). Seven assigned[50] slowly exchanging peptide NHs of *Nm*HO-PH-H_2O in ^2H_2O solution (residues 112-113, 182-184) also exhibit exchange peaks at pH 10.5 to their counterparts in *Nm*HO-PH-OH (Figure 8).

Dipolar contacts within *Nm*HO-PH-OH

NOESY contacts among protons within the *Nm*HO-PH-OH complex are most readily identified for protons first identified by magnetization exchange from *Nm*HO-PH-H_2O. The sequential N_i-N_{i+1} contacts at pH 10.5 within the *Nm*HO-PH-OH complex for Tyr112-Glu115 and Ala182-Tyr184 are observed (Figure 8A), once the exchange cross peaks between the H_2O and OH^- complexes are identified (Figure 7). Hence, these peptide NHs exhibit long $^1H \rightarrow {}^2H$ exchange lifetimes of over a period of several days even at pH 10.5. Also shown in Figure 8 are the exchange cross peaks for the nearly degenerate His53 ring $C_{\delta 1}H$ and $C_{\varepsilon 2}H$ (in *Nm*HO-PH-H_2O[50]) to their well-resolved positions in *Nm*HO-PH-OH (Figure 8A), and the exchange cross peaks for the key His141 $C_{\delta 2}H$ (Figure 8C).

The separate exchange cross peaks for the Tyr184 ring (Figure 8A), when projected to the diagonal (Figure 8B), identify the intramolecular NOESY cross peak for the Tyr184 ring within the *Nm*HO-PH-OH complex, as well as the expected intramolecular Tyr184 $C_\delta Hs$ to NH cross peaks (Figure 8A). Saturation of the resolved $3CH_3$ peak of the *Nm*HO-PH-OH complex at pH 10.5 (Figure 8D) yields the NOE difference-spectrum with the expected cross peaks to both ring protons of Tyr184, as well as to the $C_\delta H$ of Phe52, whose exchange cross peak with the same ring proton in *Nm*HO-PH-H_2O (marked*) is now also observed. The $3CH_3$ exhibited very similar NOE patterns in both *Nm*HO-PH-CN [34] and *Nm*HO-PH-H_2O. [50]

Anisotropy and orientation of the paramagnetic susceptibility tensor χ

The magnetic anisotropy of d_π, low-spin iron(III) is large, positive [38, 45, 49] and primarily axial ($|\Delta\chi_{ax}/\Delta\chi_{rh}|$~3), with $\Delta\chi_{ax}$ ~2.5×10^{-8} m^3/mol. In contrast, the magnetic anisotropy of high-spin *Nm*HO-PH-H_2O is also largely axial, [50] but negative with $\Delta\chi_{ax}$ ~-2.0×10^{-8} m^3/mol. In Table 2 we list the observed dipolar shift, δ_{dip}(obs), obtained via Eq. (1) for protons on residues with δ_{dip}(obs) > |0.25| ppm for *Nm*HO-PH-OH, and compare these data with the previously reported data for the high-spin [50] *Nm*HO-PH-H_2O with negative $\Delta\chi_{ax}$, and low-spin [34] *Nm*HO-PH-CN with positive $\Delta\chi_{ax}$. It is apparent that in each case the *sign of the dipolar*

shift in *Nm*HO-PH-OH is the same as that in *Nm*HO-PH-CN, and opposite in sign to that in *Nm*HO-PH-H_2O, dictating that $\Delta\chi_{ax}$ is *positive* in *Nm*HO-PH-OH.

We first address the relative importance of the $\Delta\chi_{ax}$ and $\Delta\chi_{rh}$ term in describing the observed dipolar shift for *Nm*HO-PH-CN. The strong dominance of the axial anisotropy over the observed dipolar shifts in *Nm*HO-PH-CN is evidenced by the fact that the change in $\Delta\chi_{ax}$ and its orientation are only weakly affected by setting $\Delta\chi_{rh} = 0$. Thus, a five-parameter search ($\Delta\chi_{ax}$, $\Delta\chi_{rh}$, α, β and $\kappa = \alpha + \gamma$) (not shown; see Supporting Information) for *Nm*HO-PH-CN yields $\Delta\chi_{ax} = 2.48 \times 10^{-8}$ m^3/mol, $\Delta\chi_{rh} = -0.52 \times 10^{-8}$ m^3/mol, α = 280 ±10°, β = 8±1°, κ = 40 ± 10°. When $\Delta\chi_{rh}$ is set equal to zero for *Nm*HO-PH-CN (making γ or κ irrelevant), the resulting three-parameter search ($\Delta\chi_{ax}$, α and β) yields: $\Delta\chi_{ax} = 2.40 \times 10^{-8}$ m^3/mol, α = 260±10° and β = 4 ±1°; (data not shown; see Supporting Information). This relative insensitivity of the axial anisotropy and its orientation to $\Delta\chi_{rh}$ in *Nm*HO-PH-CN is due to the fact that the heme occupies most of the space that is strongly influenced by the rhombic term in Eq. (1), such that the δ_{dip} for non-ligated residues are reasonably well modeled by a solely $\Delta\chi_{ax}$ value insignificantly different from the true $\Delta\chi_{ax}$. It is reasonable that $\Delta\chi_{ax}$ will similarly dominate the dipolar shifts in *Nm*HO-PH-OH.

Using the δ_{dip}(obs) for assigned protons for *Nm*HO-PH-OH listed in Table 2 as input for a least-square determination, of initially $\Delta\chi_{ax}$ ($\Delta\chi_{rh} = 0$, $\alpha = \beta = 0$) normal to the heme, yielded a good fit with $\Delta\chi_{ax} = 1.04 \pm 0.10 \times 10^{-8}$ m^3/mol (not shown). Relaxing the restriction of the major magnetic axis normal to the heme, the three-parameter fit ($\Delta\chi_{ax}$, α, β) yielded essentially the same $\Delta\chi_{ax} = 1.05 \pm 0.10 \times 10^{-8}$ m^3/mol, with a very small tilt β = 4±1° in a direction with α = 260 ±15°, an inconsequentially reduced residual error function, and a reasonable correlation between δ_{dip}(obs) and δ_{dip}(calc), as shown in Figure 9. Moreover, the optimized magnetic axes do not predict any hyperfine shifted signal which should partially resolved either on the diamagnetic envelope edges or in the small window between the aromatic and aliphatic protons. Hence we conclude that the magnetic anisotropy of *Nm*HO-PH-OH is predominantly axial, clearly positive in sign, and ~40% of the magnitude of that in *Nm*HO-PH-CN.[34] These results are consistent only with the primary population of the d_π (or $d_{xy}{}^2(d_{xz},d_{yz})^3$)ground state.

Influence on H-bond strength

Low-field bias of labile proton diamagnetic chemical shifts has been shown to correlate with H-bond length, and hence H-bond strength. [59, 60] However, in order to compare the different derivatives of *Nm*HO, the observed chemical shift, δ_{DSS}(obs), must be corrected for the contribution from the paramagnetism, δ_{dip}(calc), obtained via the magnetic axes derived above. Hence δ_{DSS}(dia*) is obtained via:

$$\delta_{DSS}(\text{dia}*)=\delta_{DSS}(\text{obs})\,\delta_{dip}(\text{calc}). \quad (4)$$

where δ_{DSS}(dia*) reflects the H-bond effects. The δ_{DSS}(obs) and δ_{DSS}(dia*) values obtained for assigned labile protons in *Nm*HO-PH-OH are listed in Table 1, where they can be compared to previously reported [50] δ_{DSS}(dia*) values for the *Nm*HO-PH-H_2O complex.

DISCUSSION

Resonance assignments

The dominance of exchange cross peaks at all pHs at which there is more than ~10% *Nm*HO-PH-OH dramatically limits the *de-novo* assignment of residues within the *Nm*HO-PH-OH complex at any pH where the sample is reasonably stable to degradation over 24 h. However, because the exchange cross peaks appear only upon increasing the pH above pH 7.0, it is possible to transfer to *Nm*HO-PH-OH, by exchange, the assignment of peaks previously[50]

assigned which are resolved or exhibit large dipolar shifts in the *Nm*HO-PH-H_2O complexes.[50] This naturally restricts residue assignments in *Nm*HO-PH-OH to those residues which in *Nm*HO-PH-H_2O exhibited significant dipolar shifts or exhibited stronger than usual H-bonds. Fortunately, these are precisely the target residues for describing the magnetic properties and H-bond interactions in *Nm*HO-PH-OH. While assignment of residues in the homologous *Pa*HO complex have not been reported, the heme signals exhibit[40] similarly slow exchange between the H_2O and OH^- complexes, such that a similar assignment strategy would be applicable.

Thermodynamics/dynamics of the $H_2O \Leftrightarrow OH^-$ transition

The integration of heme methyl peaks in the H_2O and OH^- complexes leads to the Henderson-Hasselbach plot in Figure 4. Integration of a high-spin and low-spin resolved methyl peak indicate that 1:1 population occurs at pH 9.8 in ^2H_2O (uncorrected for isotope effect), and about 0.4 units lower in ^1H_2O, ~9.4 (based on integration of the pH 10.2 spectra in ^1H_2O). The apparent pK for *Nm*HO is some 1.5-1.8 units higher than values reported for the homologous *Pa*HO complex (~8.0-8.3).[13, 40] The obvious conclusion is that the H_2O complex is stabilized, and/or the OH^- complex is destabilized,[41] in *Nm*HO relative to *Pa*HO substrate complexes. Comparison of the axial field strengths via $\Delta\chi_{ax}$ and D,[61] the zero-field splitting parameter,[50] in the two HO-PH-H_2O complexes would shed some light on potential differences in ligated water H-bonding with the protein matrix for the high-spin complexes of *Pa*HO and *Nm*HO. Such data are available for the *Nm*HO complex,[50] but not yet for the *Pa*HO complex. The estimated rate of exchange $<10^3\ s^{-1}$ for the *Nm*HO-PH complex is somewhat slower than estimated for the *Pa*HO-PH complex.[40] Similarly slow exchange has been reported for the *Pa***HO**-PH-H_2O/OH pair,[40] but such slow exchange is not typical for all such HO complexes, as hHO exhibits slow exchange (Zhu, W; Ogura, H; Wong, J.-L.; Ortiz de Montellano, P. R.; La Mar, G.N.; unpublished data).

Magnetic properties and orbital ground state for *Nm*HO-PH-OH

The comparison of the sign of δ_{dip}(obs) for assigned signals of *Nm*HO-PH-OH, with the reported sign of δ_{dip}(obs) for S = 1/2, d_π *Nm*HO-PH-CN[34] ($\Delta\chi_{ax} > 0$), and S = 5/2 *Nm*HO-PH-H_2O[50] ($\Delta\chi_{ax} < 0$), in Table 2 establishes that the axial anisotropy of *Nm*HO-PH-OH is clearly positive. Quantitation of $\Delta\chi_{ax}$ leads to $\Delta\chi_{ax} = 1.04\pm0.10 \times 10^{-8}\ m^3/mol$. The retained sign but reduced magnitude of the axial anisotropy in *Nm*HO-PH-CN relative to *Nm*HO-PH-OH is consistent with the pattern of the g-values in the EPR spectra of the same metglobin complexes.[45] The sign and magnitude of $\Delta\chi_{ax}$ in *Nm*HO-PH-OH therefore support only a predominantly 'd_π' orbital ground state[38, 45]

The resolved *Nm*HO-PH-OH heme $3CH_3$ and $8CH_3$ peaks exhibit deviations from the general Curie behavior of the low-field methyl peak in the 'd_π' orbital ground state of low-spin cyanoferrihemoprotein[49, 62, 63] complexes. However, hydroxide is a significantly weaker axial field strength ligand than cyanide, and the majority of metglobin hydroxide complexes with the dominant 'd_π', S = 1/2 ground state, exhibit similar deviations from Curie behavior[49] because of the weak thermal population of the high-spin ferric state with its much larger methyl contact shifts.

The present results for *Nm*HO-PH-OH with a d_π ground state are in contrast to the 'd_{xy}' orbital ground state proposed[6, 40] for the homologous *Pa*HO-PH-OH complex on the basis of the ^{13}C contact shift pattern of the PH substrate. The significant difference in the pKs for the acid-alkaline transition in *Pa*HO and *Nm*HO complexes would allow for significant differences in the effective axial field strength of the OH^- ligand, such that different orbital ground states could, in principle, be populated for the two complexes. The relative values for the pKs for the two complexes are consistent with, but not proof for, stronger H-bond stabilization of the

ligated OH^- by proton donation by a non-ligated water in *Pa*HO than *Nm*HO (see Figure 1C). At this time, the ^{13}C analysis of PH contact shifts[40] has not been performed on *Nm*HO-PH-OH, and the sign and magnitude of the axial anisotropy have not been reported for *Pa*HO-PH-OH. Similar studies on both HOs may resolve this apparent paradox. The present data, however, indicate emphatically that, the 'd_{xy}' orbital ground state of the HO-PH-OH complex is clearly *not a signature of the general distal HO environment*.

Dynamic stability of *Nm*HO-PH-OH

It is remarkable that essentially all of the labile proton signals characterized[50] at pH 7.0 in *Nm*HO-PH-H_2O are still detectable at pH 10.2, since they usually exhibit base-catalyzed exchange.[64] Even more remarkable is the observation that saturation factors in 3:9:19 difference-spectra [52] between on-resonance and off-resonance saturation of the water signal at pH 10.2 (not shown; see Supporting Information) leads to small, and essentially the same (or smaller), saturation factors at pH 10.2 as observed at pH 7.0, where their exchange rate with bulk solvent was shown to be extremely slow.[34] Thus the high dynamic stability, as reflected in very slow exchange rates of NHs, observed near neutral pH, appears to be retained even in strongly alkaline medium.

Effect of H_2O to OH^- conversion on the distal H-bond network

Correlations of δ_{DSS}(obs) for δ_{dip}(calc) for assigned *Nm*HO-PH-OH labile protons are listed in Table 1. Also included are δ_{dip}(calc) values for *Nm*HO-PH-OH which allow determination of δ_{DSS}(dia*), and the differences in δ_{dip}(calc) between the two complex: $\Delta\delta_{dip}$(calc) = δ_{dip}(calc:*Nm*HO-PH-H_2O) - δ_{dip}(calc:*Nm*HO-PH-OH), where δ_{dip}(calc:*Nm*HO-PH-H_2O) values have been published previously.[50], and δ_{dip}(calc) for *Nm*HO-PH-OH are estimated by the magnetic axes described above. It must be noted, since both the *Nm*HO-PH-H_2O and *Nm*HO-PH-OH magnetic axes determination are based on only $\Delta\chi_{ax} \neq 0$) (*i.e.*, $\Delta\chi_{rh} = 0$), and the magnetic axes for *Nm*HO-PH-OH on the basis of significantly fewer experimental δ_{dip}(obs) than from *Nm*HO-PH-H_2O, [50] the uncertainties of $\Delta\delta_{dip}$(calc) increase with increasing δ_{dip}(calc) for either complex. Hence, we conclude that differences in δ_{DSS}(dia*) between the H_2O and OH^- complex are significant only if this difference is comparable to the magnitude of $\Delta\delta_{dip}$(calc).

Inspection of Table 1 shows that, while δ_{DSS}(obs) differs by as much as 1.6 ppm between the two complexes, correction for δ_{dip}(calc) for each complex reduces the difference in δ_{DSS}(dia*) to well under 0.2 ppm for all but a few labile protons. Hence the strength of the majority of the H-bonds is strongly conserved upon deprotonating the axial water. Among those NHs with significant (>0.2 ppm) differences in δ_{DSS}(dia*) in Table 1, Gln49 N_εHs, and Cys113 NH, each exhibit large $|\Delta\delta_{dip}$(calc)| ~1.0 to 1.3, rendering the interpretation of $\Delta\delta_{DSS}$(dia*) questionable. On the other hand, His53 $N_{\varepsilon 1}$H and Trp153 N_εH exhibit lower field bias in the OH^- than H_2O complex, by amounts that are close to the $\Delta\delta_{dip}$(calc), and hence can be considered significant. The data in Table 1 lead to the conclusion that the diamagnetic chemical shift, and hence H-bond donor strengths for His53 $N_{\varepsilon 1}$H and Trp153 N_εH, is significantly modulated by the $H_2O \Leftrightarrow OH^-$ conversion, with both H-bond donor strengths slightly greater in the OH^- than H_2O complex.

Figure 10 presents a schematic of the active site of *Nm*HO-PH-H_2O [14] that depicts the ligated H_2O (Figure 10A) or OH^- (Figure 10B) (both green spheres) and the three non-coordinated, catalytically implicated ordered water molecules (yellow spheres), as well as the residues (specifically His53) that interact directly, or indirectly, with these water molecules. The side chains of both Gln49 and His53 are rotated 180° about the β-γ bonds from that in the crystal structures [14, 15], as confirmed by solution NOESY cross peaks in both *Nm*HO-PH-CN [34] and *Nm*HO-PH-H_2O.[50] Arrows depict H-bond direction for cases where the position of the donor

and acceptor atoms are clear. Dashed lines represent the other H-bonds for which it is not possible, based on either crystallography or ^{1}H NMR, to uniquely ascertain the direction of the proton donation. Conversion of the necessarily H-bond donor (Figures 1B and 10A) ligated water#1 to a necessarily H-bond acceptor hydroxide molecule (Figures 1C and 10B) logically leads to a stronger H-bond donation by His53 $N_{\varepsilon 1}H$ for the ligated OH^- as observed.

Trp153 $N_\varepsilon H$ in *Nm*HO-PH-H_2O serves as a H-bond donor primarily to an ordered water molecule #44, which, in turn, H-bonds to another ordered water molecule #32 that is a donor to the carboxylate of the 6-propionate. [14] Increasing the negative change on the heme by deprotonating the axial water could lead to the propionate anion carboxylate serving as a stronger H-bond acceptor to the ordered water #32, with the effect further transmitted to the Trp153 $N_\varepsilon H$. The δ_{DSS}(dia*) values for Gln49 N_δHs chemical shifts, and hence H-bond strength of the side chain, appear also to respond to $H_2O \rightarrow OH^-$ conversion, but the chemical shift difference is much less than the $\Delta\delta_{dip}$(calc). The further quantitation of $\Delta\chi_{rh}$ for *Nm*HO-PH-OH would assist in more accurately defining the change in H-bond strength. While additional assignments in *Nm*HO-PH-OH by ^{1}H NMR may be problematical due to the high pK and the inability to predominantly populate the *Nm*HO-PH-OH complex, the use of electron withdrawing substitutions is known[42-44] to markedly lower the acid-alkaline pK, and hence could allow a complete conversion to the hydroxide complex below pH 10 without danger of degradation at the extreme pH. Similar ^{1}H NMR studies of the hydroxide complex of a formyl-substituted substrate are planned.

The data show that the state of the axial water is transmitted to the His53 side chain $N_{\varepsilon 1}H$ some 10Å from the iron. Since the primary interaction of the iron ligand is with one (#37) of the ordered water molecules, which is linked to His53 by an additional two ordered water molecules (#243 and #77), it is reasonable that this “link” between the ligand and His53 is transmitted via the water-chain. The small effect on His53 $N_{\varepsilon 1}H$, and the absence of clear perturbations of other H-bonds in the distal network (*i.e.*, His141, Gln49) by the H_2O to OH^- conversion may be considered surprising, in view of the dramatic acid/base properties of the alternate heme iron ligands. However, each of these residues, as well as the catalytic water molecules shown in Figure 10, are members of a much more extended network of H-bonds, and ordered water molecules, [15, 34] such that this highly coupled network may compensate for a single strong perturbation within the network. The further characterization of the H-bond/ordered water network must await planned ^{15}N-labeling of *Nm*HO.

CONCLUSIONS

The assignment of active site residues in ferric, low-spin, *Nm*HO-PH-OH reveals a pattern of dipolar shifts for active site residues that is consistent with only positive axial anisotropy for the paramagnetic susceptibility tensor. Quantitation of the tensor yields an axial anisotropy with ~40% of the magnitude found in the well-characterized ferric, low-spin *Nm*HO-PH-CN complex.[34] Hence the dominant orbital ground state for *Nm*HO-PH-OH is the common d_π, and not the unusual ‘d_{xy}’ orbital state suggested to be a signature of the HO active site. The conversion of the H-bond donor ligated water to the H-bond acceptor ligated hydroxide leads to a detectable strengthening of the His53 side chain H-bond, which is linked to the ligated water/hydroxide through three ordered water molecules.

Supplementary Material

Refer to Web version on PubMed Central for supplementary material.

Acknowledgements

This work was supported, in part, by the National Institutes of Health, GM62830 (GNL) and a grant-in-Aid for Scientific Research (16570102) from the Ministry of Education and Sports, Science and Teaching, Japan (T.Y.)

References

1. Tenhunen R, Marver HS, Schmid R. J Biol Chem 1969;244:6388–6394. [PubMed: 4390967]
2. Yoshida T, Migita CT. J Inorg Biochem 2000;82:33–41. [PubMed: 11132636]
3. Wilks A. Antioxid Redox Signal 2002;4:603–614. [PubMed: 12230872]
4. Ortiz de Montellano, PR.; Auclair, K. The Porphryin Handbook. Kadish, KM.; Smith, KM.; Guilard, R., editors. 12. Elsevier Science; San Diego, CA: 2003. p. 175-202.
5. Frankenberg-Dinkel N. Antoxid Redox Signal 2004;6:825–834.
6. Rivera M, Zeng Y. J Inorg Biochem 2005;99:337–354. [PubMed: 15598511]
7. Uzel C, Conrad ME. Seminars in Hematology 1998;35:27–34. [PubMed: 9460807]
8. Maines MD. Ann Rev Pharmacol Toxicol 1997;37:517–554. [PubMed: 9131263]
9. Verma A, Hirsch DJ, Glatt CE, Ronnett GV, Snyder SH. Science 1993;259:381–384. [PubMed: 7678352]
10. Beale SI. Ciba Found Symp 1994;180:156–168. [PubMed: 7842851]
11. Wilks A, Schmitt MP. J Biol Chem 1998;273:837–841. [PubMed: 9422739]
12. Zhu W, Willks A, Stojiljkovic I. J Bacteriol 2000;182:6783–6790. [PubMed: 11073924]
13. Ratliff M, Zhu M, Deshmukh R, Wilks A, Stojiljkovic I. J Bacteriol 2001;183:6394–6403. [PubMed: 11591684]
14. Schuller DJ, Zhu W, Stojiljkovic I, Wilks A, Poulos TL. Biochemistry 2001;40:11552–11558. [PubMed: 11560504]
15. Friedman JM, Lad L, Deshmukh R, Li HY, Wilks A, Poulos TL. J Biol Chem 2003;278:34654–34659. [PubMed: 12819228]
16. Caignan GA, Deshmukh R, Wilks A, Zeng Y, Huang H-W, Moenne-Loccoz P, Bunce RA, Eastman MA, Rivera M. J Am Chem Soc 2002;124:14879–14892. [PubMed: 12475329]
17. Friedman J, Lad L, Li H, Wilks A, Poulos TL. Biochemistry 2004;43:5239–5245. [PubMed: 15122889]
18. Ortiz de Montellano PR, Wilks A. Adv Inorg Chem 2001;51:359–407.
19. Yoshida T, Noguchi M, Kikuchi G. J Biol Chem 1980;255:4418–4420. [PubMed: 6892813]
20. Wilks A, Torpey J, Ortiz de Montellano PR. J Biol Chem 1994;269:29553–29556. [PubMed: 7961940]
21. Ortiz de Montellano PR. Acct Chem Res 1998;31:543–549.
22. Davydov RM, Yoshida T, Ikeda-Saito M, Hoffman BM. J Am Chem Soc 1999;121:10656–10657.
23. Davydov R, Kofman V, Fujii H, Yoshida T, Ikeda-Saito M, Hoffman BM. J Am Chem Soc 2002;124:1798–1808. [PubMed: 11853459]
24. Davydov R, Chemerisov S, Werst DE, Rajh T, Matsui T, Ikeda-Saito M, Hoffman BM. J Am Chem Soc 2004;126:15960–15961. [PubMed: 15584719]
25. Kamachi T, Shestakov AF, Yoshizawa K. J Am Chem Soc 2004;126:3672–3673. [PubMed: 15038694]
26. Unno M, Matsui T, Chu GC, Coutoure M, Yoshida T, Rousseau DL, Olson JS, Ikeda-Saito M. J Biol Chem 2004;279:21055–21061. [PubMed: 14966119]
27. Lad L, Wang J, Li H, Friedman J, Bhaskar B, Ortiz de Montellano PR, Poulos TL. J Mol Biol 2003;330:527–538. [PubMed: 12842469]
28. Sugishima M, Sakamoto H, Noguchi M, Fukuyama K. Biochemistry 2003;42:9898–9905. [PubMed: 12924938]
29. Gorst CM, Wilks A, Yeh DC, Ortiz de Montellano PR, La Mar GN. J Am Chem Soc 1998;120:8875–8884.

30. La Mar GN, Asokan A, Espiritu B, Yeh DC, Auclair K, Ortiz de Montellano PR. J Biol Chem 2001;276:15676–15687. [PubMed: 11297521]
31. Li Y, Syvitski RT, Auclair K, Wilks A, Ortiz de Montellano PR, La Mar GN. J Biol Chem 2002;277:33018–33031. [PubMed: 12070167]
32. Li Y, Syvitski RT, Auclair K, Ortiz de Montellano PR, La Mar GN. J Am Chem Soc 2003;125:13392–13403. [PubMed: 14583035]
33. Li Y, Syvitski RT, Chu GC, Ikeda-Saito M, La Mar GN. J Biol Chem 2003;279:6651–6663. [PubMed: 12480929]
34. Liu Y, Zhang X, Yoshida T, La Mar GN. Biochemistry 2004;43:10112–10126. [PubMed: 15287739]
35. Schuller DJ, Wilks A, Ortiz de Montellano PR, Poulos TL. Nature Struct Biol 1999;6:860–867. [PubMed: 10467099]
36. Sugishima M, Sakamoto H, Higashimoto Y, Omata Y, Hayashi S, Noguchi M, Fukuyama K. J Biol Chem 2002:45086–45090. [PubMed: 12235152]
37. Hirotsu S, Chu GC, Unno M, Lee D-S, Yoshida T, Park S-Y, Shiro Y, Ikeda-Saito M. J Biol Chem 2004;279:11937–11947. [PubMed: 14645223]
38. Walker, FA. The Porphyrin Handbook. Kadish, KM.; Smith, KM.; Guilard, R., editors. 5. Academic Press; Boston: 2000. p. 1-183.
39. Rivera M, Caignan GA, Astashkin AV, Raitsimring AM, Shokhireva TK, Walker FA. J Am Chem Soc 2002;124:6077–6089. [PubMed: 12022842]
40. Caignan GA, Deshmukh R, Zeng Y, Wilks A, Bunce RA, Rivera M. J Am Chem Soc 2003;125:11842–11852. [PubMed: 14505406]
41. Caughey, WS. Hemes and Hemoproteins. Chance, B.; Estabrook, RW.; Yonetani, T., editors. Academic Press; New York: 1966. p. 276-277.
42. Brunori M, Amiconi G, Antonini E, Wyman J, Zito R, Rossi-Fanolli A. Biochem Biophys Acta 1968;154:315–322. [PubMed: 5637052]
43. Cowgill RW, Clark WM. J Biol Chem 1952;198:33–61. [PubMed: 12999715]
44. McGrath TM, La Mar GN. Biochim Biophys Acta 1978;534:99–111. [PubMed: 26418]
45. Palmer, G. The Porphyrins. Dolphin, D., editor. IV. Academic Press; New York: 1979. p. 313-353.
46. Walker FA, Simonis U. Biol Magn Reson 1993:12.
47. Williams G, Clayden NJ, Moore GR, Williams RJP. J Mol Biol 1985;183:447–460. [PubMed: 2991533]
48. Emerson SD, La Mar GN. Biochemistry 1990;29:1556–1566. [PubMed: 2334714]
49. La Mar, GN.; Satterlee, JD.; de Ropp, JS. The Porphyrins Handbook. Kadish, KM.; Smith, KM.; Guilard, R., editors. 5. Academic Press; San Diego: 2000. p. 185-298.
50. Liu Y, Zhang X, Yoshida T, La Mar GN. J Am Chem Soc 2005;127:6409–6422. [PubMed: 15853349]
51. Johnston PD, Figueroa N, Redfield AG. Proc Natl Acad Sci USA 1979;76:3130–3134. [PubMed: 386331]
52. Piotto M, Sandek V, Sklenar V. J Biomol NMR 1992;2:661–666. [PubMed: 1490109]
53. Jeener J, Meier BH, Bachmann P, Ernst RR. J Chem Phys 1979;71:4546–4553.
54. Griesinger C, Otting G, Wüthrich K, Ernst RR. J Am Chem Soc 1988;110:7870–7872.
55. Bax A, Davis DG. J Magn Reson 1985;65:355–360.
56. Neal S, Nip AM, Zhang H, Wishart DS. J Biomol NMR 2003;26:215–240. [PubMed: 12766419]
57. Cross KJ, Wright PE. J Magn Reson 1985;64:220–231.
58. Sandström, J. Dynamic NMR Spectroscopy. Academic Press; New York: 1982.
59. Wagner G, Pardi A, Wüthrich K. J Am Chem Soc 1983;105:5948–5949.
60. Harris TK, Mildvan AS. Prot: Struct Funct Genet 1999;35:275–282.
61. Brackett GC, Richards DL, Caughey WS. J Chem Phys 1971;54:4383–4401.
62. Turner DL. J Magn Reson 1993;104:197–202.A
63. Shokhirev NV, Walker FA. J Phys Chem 1995;99:17795–17804.
64. Englander SW, Kallenbach NR. Quart Rev Biophys 1984;16:521–655.

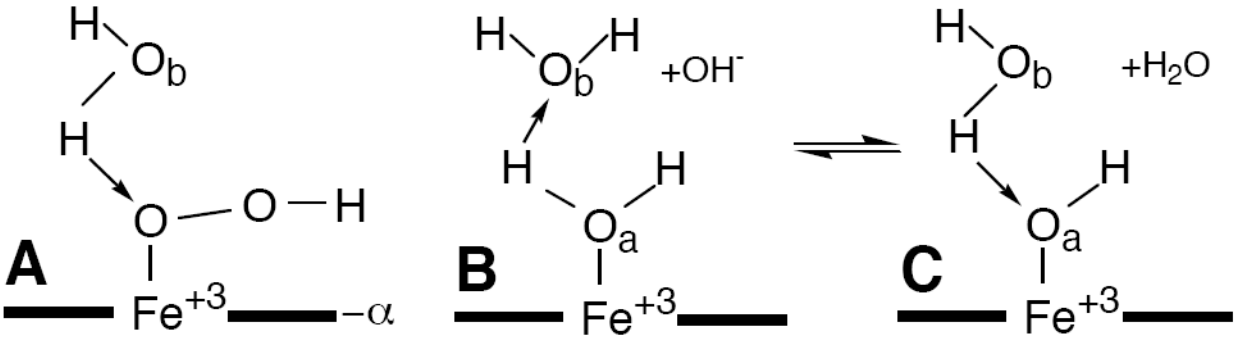

Figure 1.

Geometry of a ferric porphyrin ligated: (**A**) hydroperoxide; (**B**) neutral water molecule *a*; and (**C**) hydroxide. The latter two species are at equilibrium at any solution pH value; this equilibrium shifts to the right with increasing pH. Non-ligated water molecule (*b*) in the distal pocket provides the major interaction for the axially ligated water molecule [14] serving as a donor to molecule b (**B**). Both the hydroperoxide (**A**), and hydroxide (**C**) serve as acceptors to water *b*.

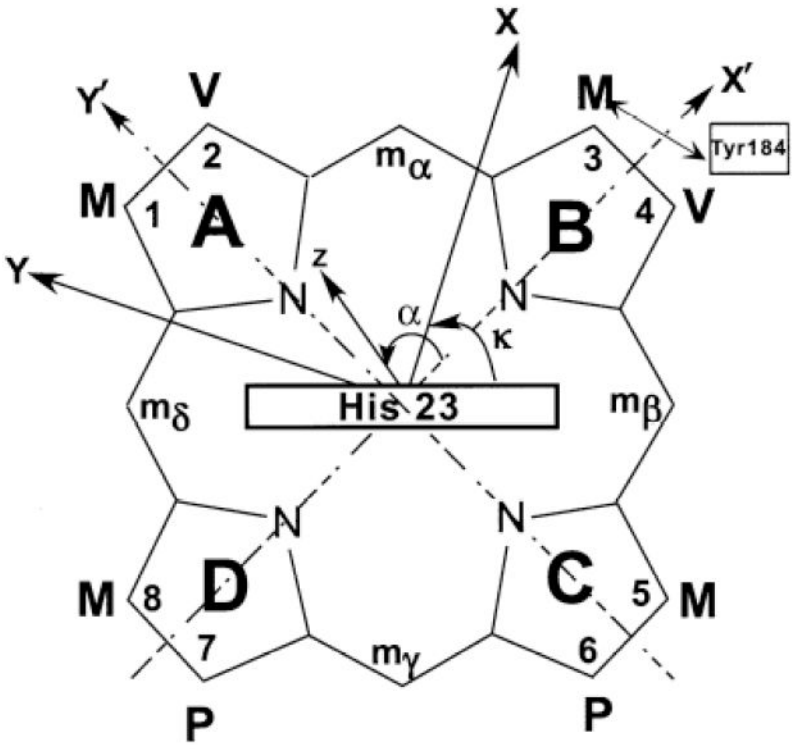

Figure 2.

Schematic structure of the heme pocket of *Nm*HO-PH-H_2O, viewed from the proximal side, showing the numbering of the protoheme (PH) skeleton, the orientation of the axial His23 imidazole plane, and the position of Tyr184 relative to pyrrole B. Also shown is the arbitrary, iron-centered reference coordinate system, x', y', z', where x', y' are in the heme plane passing through pyrrole N_B, N_A, respectively and z' points to the proximal side. The magnetic coordinate system, x, y, z, for an axially anisotropic paramagnetic susceptibility tensor, χ, where χ is diagonal, is defined by a tilt from the unique or z axis from the heme normal (z' axis) by an angle β (not shown), and in a direction defined by the angle α between the projection of z on the x', y' plane and the x' axis.

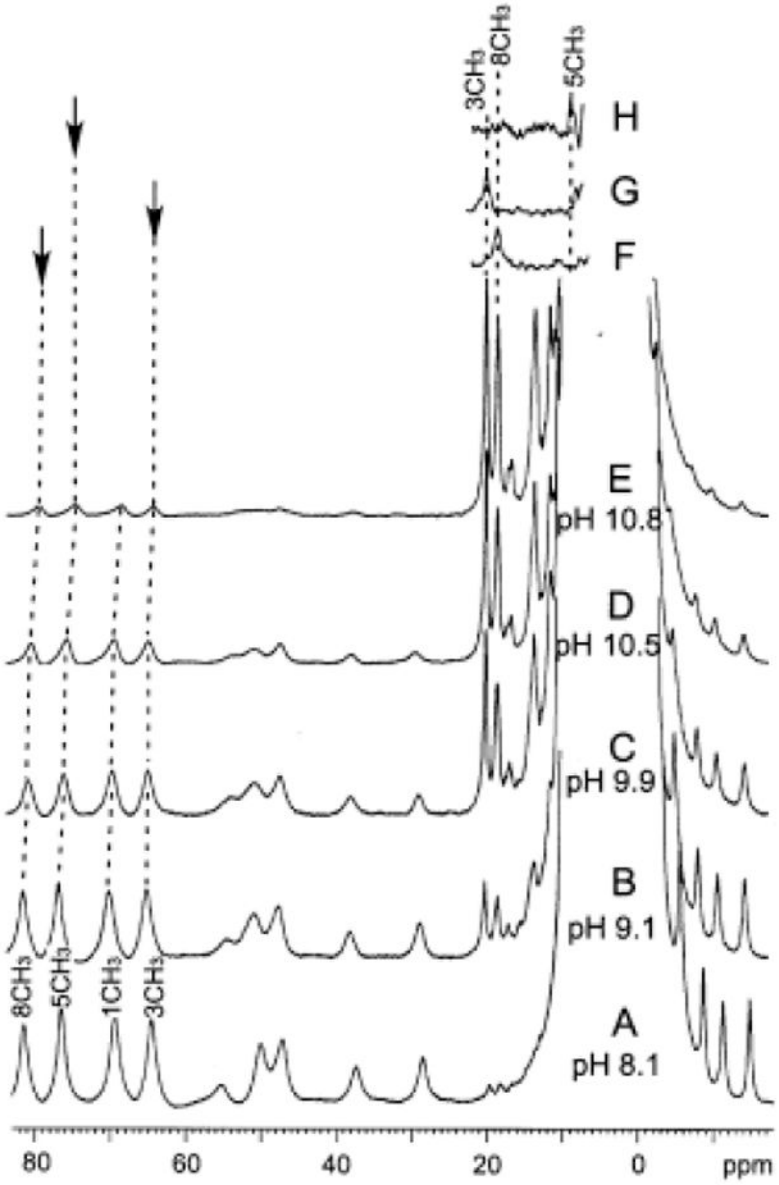

Figure 3.

Resolved portions of the 500 MHz ^{1}H NMR spectrum of *Nm*HO-PH-H_2O/OH at 25°C as a function of solution pH. The predominant *Nm*HO-PH-H_2O complex with its assigned residues is shown at (**A**) pH 8.1; (**B**) pH 9.1; (**C**) pH 9.9; (**D**) pH 10.5 (6%:94% *Nm*HO-PH-H_2O:*Nm*HO-PH-OH) and (**E**) pH 10.8. The magnetization-transfer difference spectra for *Nm*HO-PH-OH upon saturating the assigned *Nm*HO-PH-H_2O heme methyl ^{50} (as indicated by vertical arrow) are shown for the (**F**) 8-CH_3, (**G**) 3-CH_3; and (**H**) 5-CH_3.

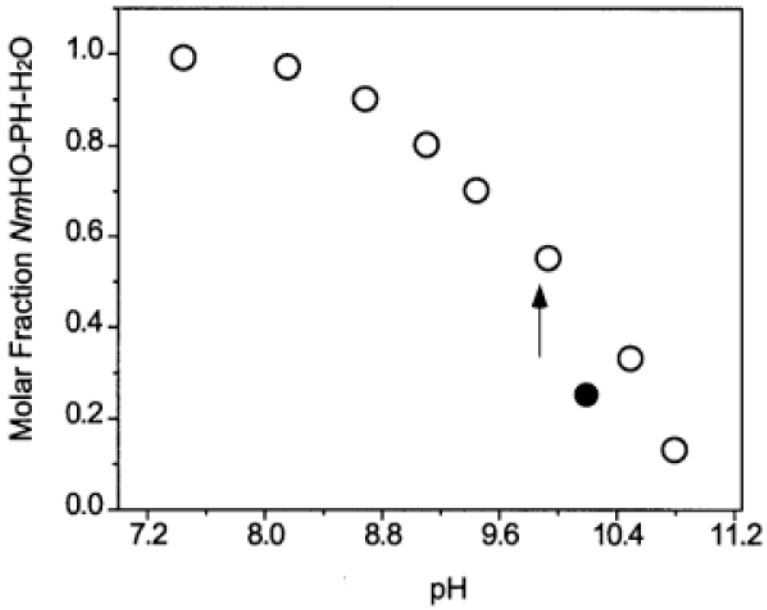

Figure 4.

A Henderson-Hasselbalch plot (mole fraction *Nm*HO-PH-OH in *Nm*HO-PH-H_2O/*Nm*HO-PH-OH mixtures as a function of pH) in ^2H_2O solution, at 25°C, as determined from the relative intensities of the heme 3-CH_3 signal in the two complexes. Data in ^2H_2O are shown as open circles. The estimated pK ~9.8 in ^2H_2O is shown by a vertical arrow. The single data point recorded in ^1H_2O solution at pH 10.2 is shown as a closed circle.

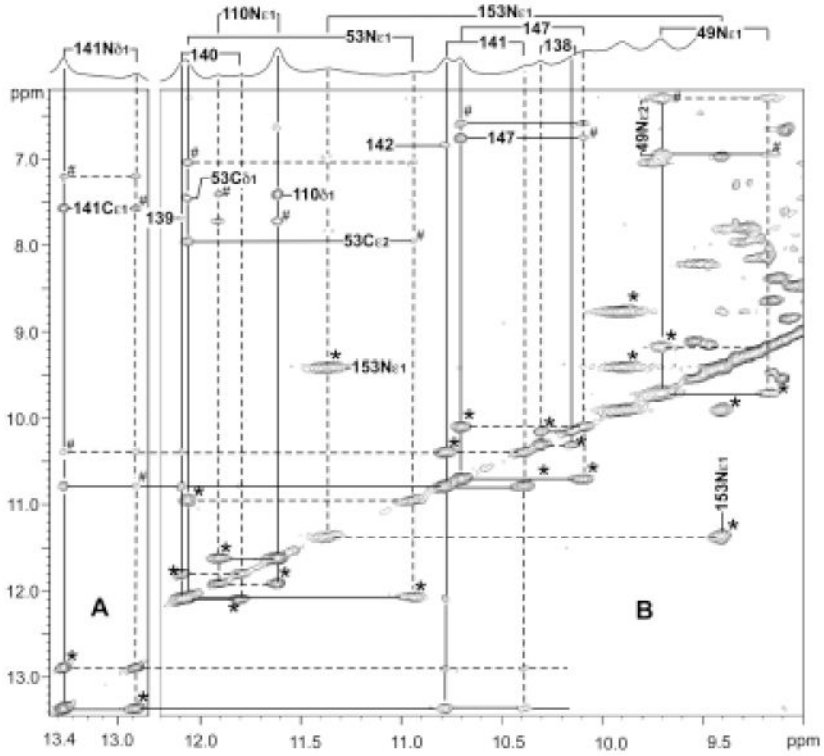

Figure 5.

Low-field resolved portion of the 600 MHz ^{1}H NMR reference spectrum of ~20% *Nm*HO-PH-H_2O; ~80% *Nm*HO-PH-OH in ^1H_2O at pH 10.2 and 25°C with bars to connect the position of the two exchanging peaks, as previously assigned for the *Nm*HO-PH-H_2O complex. (**A**, **B**) provide the pertinent portion of the 600 MHz NOESY/EXSY spectrum (mixing time 40 ms, repetition rate 2 s^{-1}) illustrating the NOESY, and exchange (EXSY; peaks marked by *) and exchange-transferred NOESY peaks (marked by #) among the low-field labile protons. The unambiguous assignment of the labeled peaks for *Nm*HO-PH-OH is completely dependent on the previous unambiguous assignments carried out on essentially pure *Nm*HO-PH-H_2O. [50] Again, protons in *Nm*HO-PH-H_2O are shown by dashed lines, while those in *Nm*HO-PH-OH are shown by solid lines. Signals are identified by residue number and position, except peptide NHs, which are labeled solely by residue number.

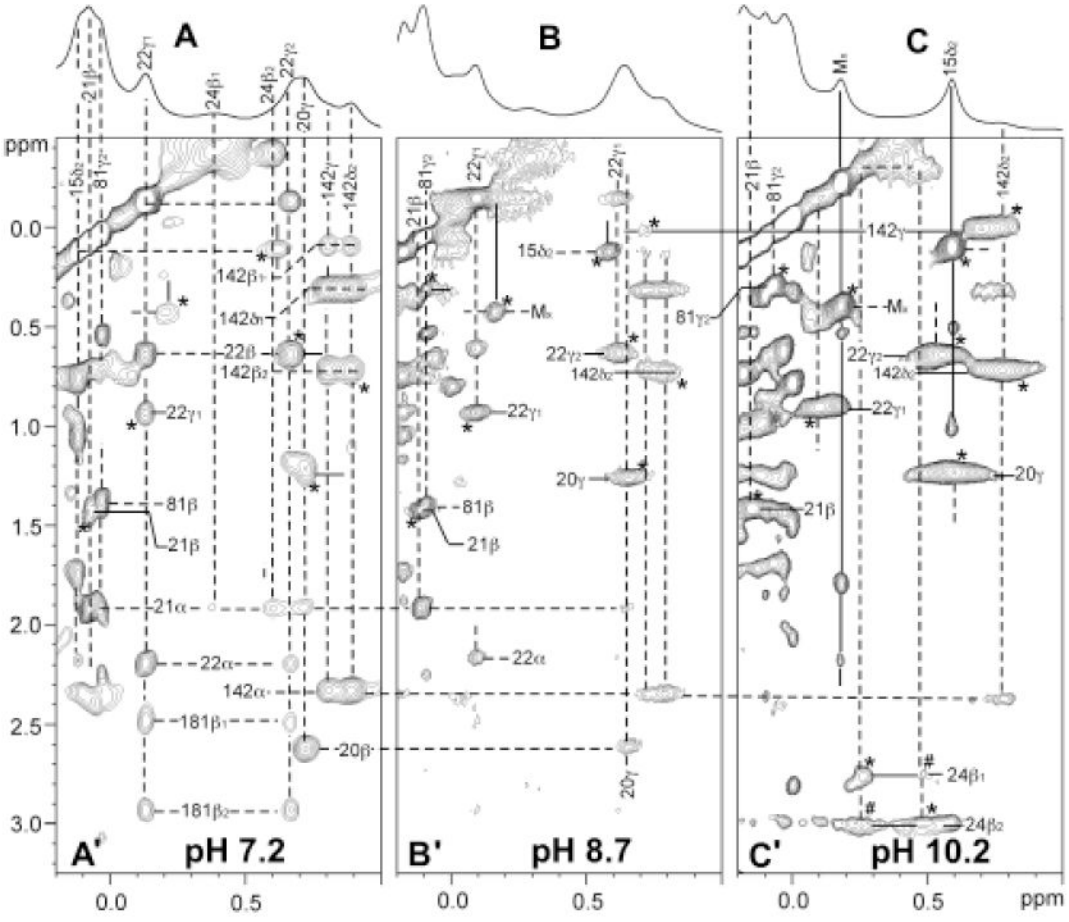

Figure 6.

Resolved upfield portion of the 600 MHz ^{1}H NMR spectrum of *Nm*HO-PH-H_2O/OH in $^{2}H_2O$ at 25°C at: (**A**) pH 7.2; (**B**) pH 8.7; and (**C**) pH 10.2 illustrating the conversion of primarily *Nm*HO-PH-H_2O in **A** to primarily *Nm*HO-PH-OH in **C**. The pertinent portions of the 600 MHz ^{1}H NMR NOESY(EXSY) spectra (mixing time 40 ms, repetition rate 2 s^{-1}) are shown in (**A**'), (**B**'), (**C**') at the pH values corresponding to the reference spectra in A, B, C, respectively. Proton frequencies are labeled by residue number and position; peptide NHs are labeled solely by number. Dashed lines identify protons in *Nm*HO-PH-H_2O assigned previously, while solid lines identify newly assigned protons in *Nm*HO-PH-OH. Asterisks identify exchange peaks and # identify exchange-transferred NOEs. Note weak exchange peak Leu15 $C_{\delta 2}H_3$ and M_X (unassigned methyls) even at pH 7.2 (**A'**), which become stronger at both pH 8.7 (**B'**) and 10.2 (**C'**). Also note diminishing intensity of intramolecular NOESY cross peaks within *Nm*HO-PH-H_2O, and increasing intensity of exchange cross peak between *Nm*HO-PH-H_2O and *Nm*HO-PH-OH with increasing pH.

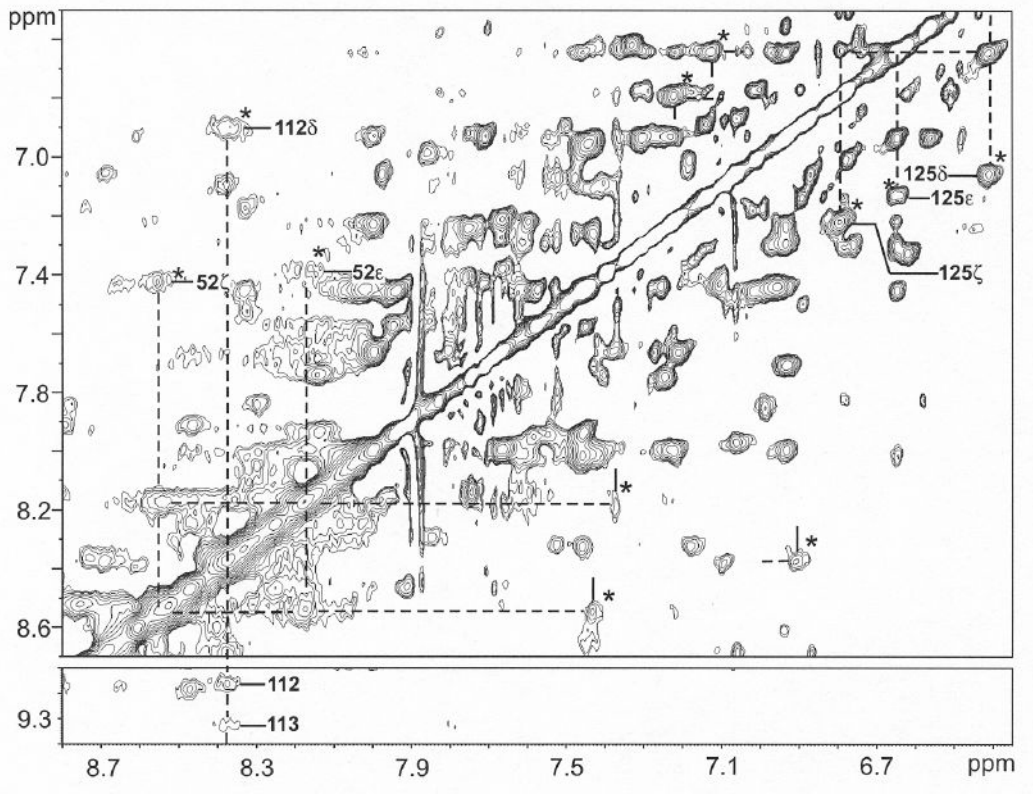

Figure 7.

Aromatic proton portion of the 600 MHz ^{1}H NMR NOESY/EXSY spectrum (mixing time 40 ms; repetition rate 2 s^{-1}) for ~85% *Nm*HO-PH-H_2O and ~15% *Nm*HO-PH-OH at pH 8.7 in $^{2}H_2O$ solution, 50 mM in phosphate at 25°C. New exchange peaks are marked by * for assigned aromatic rings in *Nm*HO-PH-H_2O and labeled for Phe52, Tyr112 and Phe125. Protons in *Nm*HO-PH-H_2O and *Nm*HO-PH-OH are shown by dashed and solid lines, respectively.

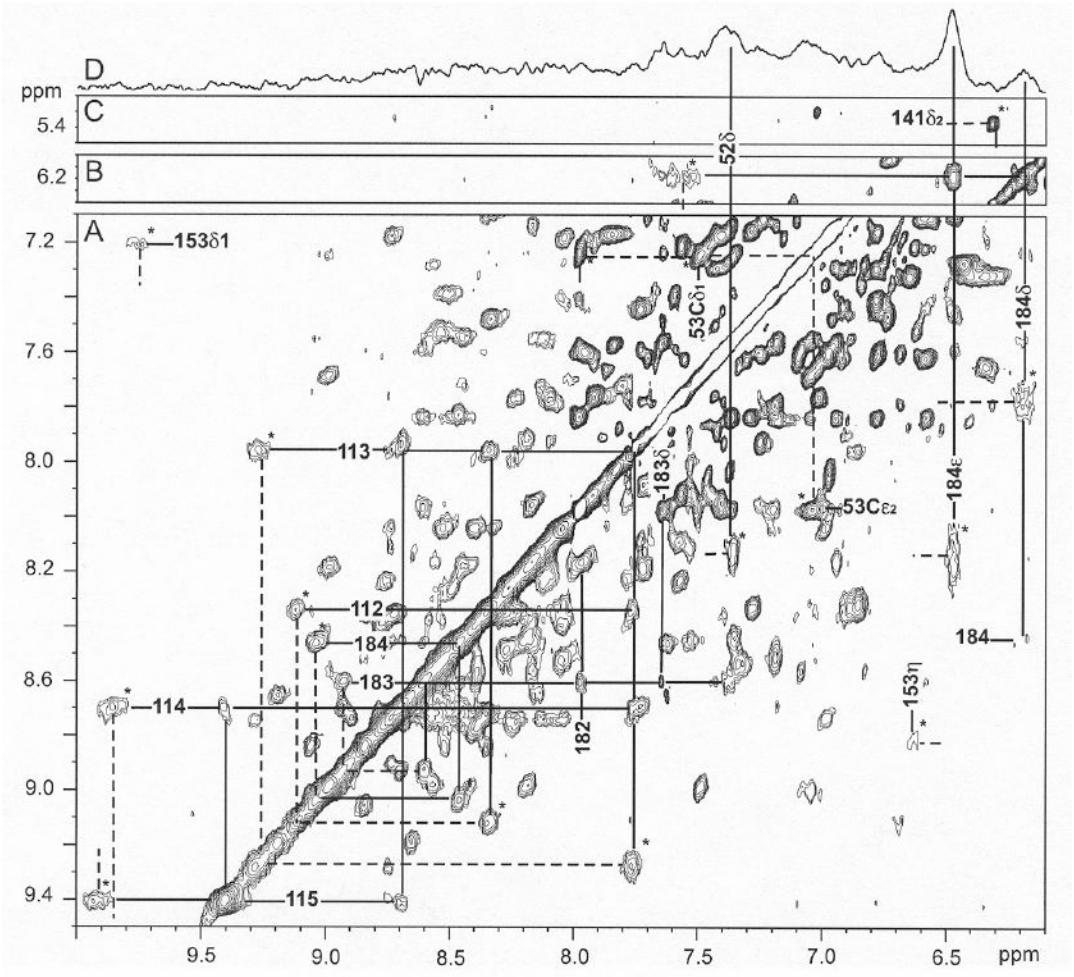

Figure 8.

Low-field portion of the ^{1}H NMR NOESY/EXSY spectrum (mixing time 40 ms; repetition rate 2 s^{-1}) of ~20% *Nm*HO-PH-H_2O, ~80% *Nm*HO-PH-OH in $^{2}H_2O$, 100 mM bicarbonate, at pH 10.5 and 25°C illustrating exchange (EXSY) cross peaks (marked by *) between *Nm*HO-PH-H_2O and *Nm*HO-PH-OH for slowly exchanging labile protons Tyr112-Gln115 and Ala182-Tyr184 (**A**), for the His53 ring $C_{\delta1}H$ and $C_{\varepsilon2}H$ (**A**), Tyr184 ring proton (**A**) and His141 $C_{\delta2}H$ (**C**). The proton frequencies of *Nm*HO-PH-H_2O and *Nm*HO-PH-OH are marked by dashed and solid lines, respectively. Note that the sequential N_i-N_{i+1} cross peaks within *Nm*HO-PH-OH are clearly observed for both helical fragments with slowly exchanging NHs. Panel (**B**) shows the intra-*Nm*HO-PH-OH Tyr184 ring NOESY cross peaks and the expected Tyr184 C_{δ}Hs to peptide NH NOESY cross peak (**A**). Panel (**D**) represents the steady-state 1D NOE difference spectrum within the *Nm*HO-PH-OH complex resulting upon saturating the 3-CH_3 of the *Nm*HO-PH-OH complex at 20 ppm, and yields the expected NOEs to the ring of Tyr184. The NOE to the Phe52 $C_{\delta}H$ arises primarily from a very strong secondary NOE via the Tyr184 ring. Note that even at this extreme alkaline pH, EXSY cross peaks are as intense as most NOESY cross peaks.

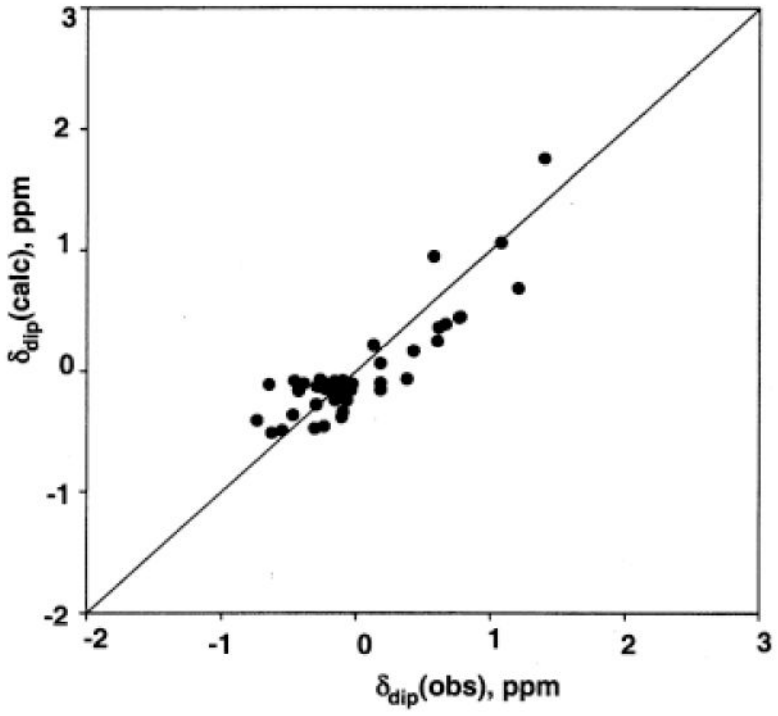

Figure 9.

Plot of δ_{dip}(obs) versus δ_{dip}(calc) for the optimized anisotropy and orientation of axially symmetric paramagnetic susceptibility tensor χ of *Nm*HO-PH-OH at 25°C, with $\alpha = 260 \pm 15°$, $\beta = 4 \pm 1°$ and $\Delta\chi_{ax} = 1.04 \pm 0.14 \times 10^{-8}$ m^3/mol. The residual error function, F/n = 0.20 ppm^2.

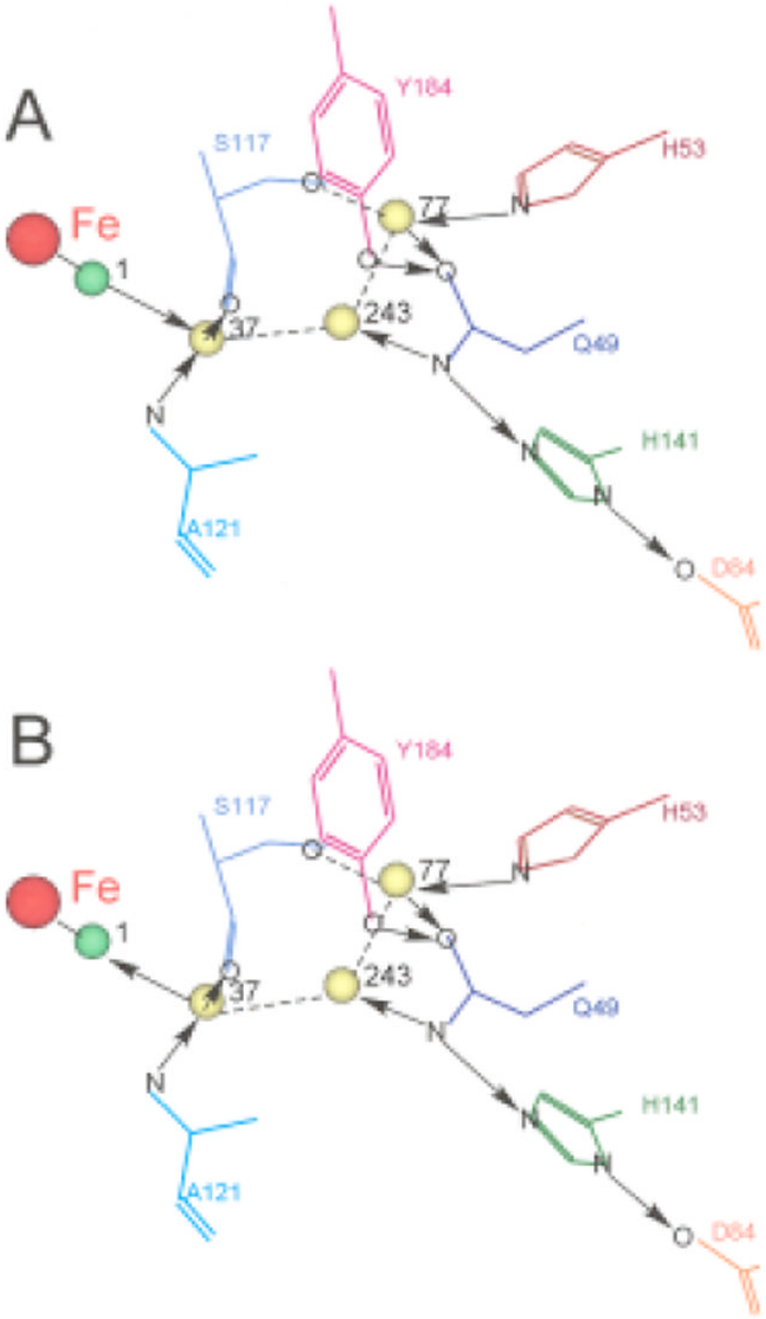

Figure 10.

(**A**) Schematic structure of the distal cavity of *Nm*HO-PH-H_2O showing the relative position of the ligated water, H_2O#1 (green sphere), the three conserved catalytically relevant, non-ligated water molecules, H_2O#243, H_2O#37 and H_2O#77 (yellow spheres) and several key residues involved in the H-bond stabilization of these water molecules based on the *Nm*HO-PH-H_2O crystal structure and the previously documented 180° rotation about the β–γ bond for the Gln49 and His53 side chain.[34, 50] The direction of H-bonds (donor → acceptor) are shown in solid arrows between the two heteroatoms. For cases where neither the crystal structure nor solution ^{1}H NMR uniquely locates the position of the proton, and hence the direction of the H-bond cannot be definitively determined, the presence of the H-bond is shown as a dashed

line. (**B**) Structure of *Nm*HO-PH-H_2O retained for the *Nm*HO-PH-OH complex, except that the H-bond direction between water #1 and water #37 is reversed from that in A. The changed direction of the axial ligand (green sphere) in converting H_2O (**A**) to OH (**B**) is consistent with the His53 $N_{\varepsilon 1}H$ serving as a strong donor upon deprotonating the water.

Table 1

Comparison of labile proton chemical shifts for *Nm*HO-PH-OH and *Nm*HO-PH-H_2O

	***Nm*HO-PH-OH**			***Nm*HO-PH-H_2O**	**Comparison**	
	δ_{DSS}(obs)[a]	δ_{dip}(calc)[b]	δ_{DSS}(dia*)[c]	δ_{DSS}(dia*)[e]	$\Delta\delta_{dip}$(calc)[d]	$\Delta\delta_{DSS}$(dia*)[f]
Peptide NHs						
Ala12	9.15	-0.09	9.24	9.31	0.29	0.07
Tyr112	8.36	-0.22	8.58	8.68	0.72	0.10
Cys113	7.75	-0.40	8.15	8.40	1.35	0.25
Ala114	8.70	-0.40	9.10	9.00	1.33	-0.10
Gln115	9.40	-0.27	9.67	9.50	0.78	-0.17
Gly138	10.30	0.05	10.25	10.28	-0.18	0.03
Ala139	7.67	0.08	7.59	7.58	-0.30	-0.01
Arg140	12.10	0.11	11.99	12.04	-0.37	0.05
His141	10.78	0.15	10.63	10.75	-0.52	0.12
Leu142	6.82	0.27	6.55	6.68	-0.92	0.13
Asp147	10.70	0.12	10.58	10.60	-0.39	0.02
Ala180	8.39	-0.11	8.50	8.42	0.44	-0.08
Phe181	8.04	-0.12	8.16	8.03	0.57	-0.13
Ala182	7.77	-0.02	7.79	7.97	0.20	0.12
Phe183	8.61	-0.08	8.69	8.65	0.35	-0.04
Tyr184	8.15	-0.19	8.34	8.51	0.73	0.17
Sidechain NHs						
Gln49 $N_{\varepsilon 1}H$	9.70	0.14	9.56	9.76	-0.72	0.20
Gln49 $N_{\varepsilon 2}H$	6.97	0.17	6.80	7.04	-1.00	0.26
His53 $N_{\varepsilon 1}H$	12.07	0.10	11.97	11.48	-0.66	-0.51
Trp110 $N_{\varepsilon}H$	11.60	-0.08	11.68	11.70	0.29	0.02
His141 $N_{\delta 1}H$	13.35	0.12	13.23	13.24	-0.48	0.01
Trp153 $N_{\varepsilon}H$	9.40	-0.36	9.76	10.54	1.25	0.82

[a] δ_{DSS}(obs), in ppm, referenced to DSS via the solvent signal, in ^1H_2O, 100 mM bicarbonate at 25°C and pH 10.2.

[b] Dipolar shift predicted by the determined magnetic axes described in Figure 8.

[c] The diamagnetic shift that reflects H-bonding differences between OH^- and H_2O complexes, as given by Eq. (4).

[d] $\Delta\delta_{dip}$(calc) = δ_{dip}(calc; *Nm*HO-PH-H_2O) - δ_{dip}(calc; *Nm*HO-PH-OH)

[e] As reported previously.[50]

[f] $\Delta\delta_{DSS}$ (dia*) = δ_{DSS}(dia*;*Nm*HO-PH-H_2O) - δ_{DSS}(dia*; *Nm*HO-PH-OH), as determined from δ_{DSS}(dia*; *Nm*HO-PH-OH) in Table 2 and δ_{DSS}(dia*; *Nm*HO-PH-H_2O) reported by Liu et al.[50]

Table 2

Chemical and dipolar shift data for strongly dipolar-shifted residues in *Nm*HO-PH-OH, *Nm*HO-PH-H_2O and *Nm*HO-PH-CN

		***Nm*HO-PH-OH**			***Nm*HO-PH-H_2O**	***Nm*HO-PH-CN**
		δ_{DSS}(obs)[a]	δ_{DSS}(dia)[b]	δ_{dip}(obs)[c]	δ_{dip}(obs)[d]	δ_{dip}(obs)[e]
Ala12	$C_\alpha H$	3.39	3.82	-0.42	0.21	-0.52
	$C_\beta H_3$	1.24	1.45	-0.23	0.42	-0.47
Thr20	$C_\gamma H_3$	1.30	0.09	1.21	-1.76	2.18
Ala21	$C_\beta H_3$	1.47	0.80	0.67	-0.65	1.24
Val22	$C_{\gamma1} H_3$	0.70	-0.07	0.77	-0.57	1.57
	$C_{\gamma2} H_3$	0.98	0.36	0.34	-0.48	1.06
Asp24	$C_{\beta1} H$	2.82	2.14	0.58	-2.51	1.51
	$C_{\beta2} H$	3.08	2.00	1.08	-2.60	2.30
Phe52	$C_\varepsilon Hs$	7.43	7.53	-0.10	0.62	-0.82
	$C_\zeta H$	7.31	7.55	-0.24	1.00	-0.15
Tyr112	$C_\delta Hs$	6.90	7.37	-0.47	0.31	-1.16
	$C_\varepsilon Hs$	-	-	-	1.00	-1.15
Cys113	$C_{\beta1} H$	2.72	3.05	-0.31	1.31	-0.71
	$C_{\beta2} H$	2.76	3.29	-0.35	1.01	-0.64
Asn118	$C_{\beta1} H$	3.12	2.42	-0.70	-2.70	1.50
	$C_{\beta2} H$	3.02	2.30	-0.62	-2.62	1.30
Ala121	$C_\beta H_3$	2.30	0.70	1.60	-4.10	4.8
Leu142	$C_{\delta2} H_3$	0.80	0.02	0.78	-0.77	(1.88)[f]
	$C_\gamma H$	0.05	0.00	0.05	-0.85	(0.94)
Trp153	$C_{\delta1} H$	6.95	7.11	-0.16	0.71	-0.14
Val157	$C_\alpha H$	2.85	3.24	-0.39	(0.30)[g]	-0.36
	$C_\beta H$	1.55	-2.01	-0.46	(0.26)	-0.35
	$C_{\gamma1} H_3$	0.37	1.02	-0.65	(0.29)	-0.38
	$C_{\gamma2} H_3$	-0.02	0.12	-0.14	(0.45)	0.55
Phe181	$C_{\beta1} H$	3.57	3.12	0.43	-0.17	0.15
	$C_{\beta2} H$	3.03	2.84	0.18	0.32	0.73
Phe183	$C_\alpha H$	4.53	4.26	-0.27	0.25	(-0.15)[g]
	$C_{\beta1} H$	3.68	3.37	-0.29	0.30	(-0.22)
	$C_{\beta2} H$	3.42	3.26	-0.16	0.40	(-0.14)
	$C_\delta Hs$	7.64	7.75	-0.11	0.21	-0.61
	$C_\varepsilon Hs$	7.37	7.62	-0.25	0.02	-0.26
Tyr184	$C_\delta Hs$	6.18	6.92	-0.74	0.62	-1.13
	$C_\varepsilon Hs$	6.48	7.07	-0.63	1.00	-1.15

[a] δ_{DSS}(obs) in ppm referenced to DSS via the solvent resonance, in ^2H_2O at pH 9.1, 100 mM in bicarbonate at 25°C.

[b] Diamagnetic chemical shift in ppm, at 25°C, calculated by the ShiftX program [56] and the *Nm*HO-PH-H_2O crystal structure.

[c] Given by Eq. (3).

[d] As reported in Ref. 50, and converted to δ_{dip}(obs) using Eq. (3) and the same δ_{DSS}(dia) as for *Nm*HO-PH-OH.

[e] As previously reported in Ref. 34, and converted to δ_{dip}(obs) by Eq. (3) and the same δDSS(dia) as for *Nm*HO-PH-OH.

[f] Not assigned in *Nm*HO-PH-CN; given in parentheses is the δ_{dip}(calc) from the published magnetic axes. [34]

[g] Not assigned in *Nm*HO-PH-H_2O; given in parentheses is the δ_{dip}(calc) from the published magnetic axes.[50]